Science Advances
AAAS

advances.sciencemag.org/cgi/content/full/5/8/eaaw8904/DC1

Supplementary Materials for

Current-driven magnetization switching in a van der Waals ferromagnet Fe_3GeTe_2

Xiao Wang, Jian Tang, Xiuxin Xia, Congli He, Junwei Zhang, Yizhou Liu, Caihua Wan, Chi Fang, Chenyang Guo,
Wenlong Yang, Yao Guang, Xiaomin Zhang, Hongjun Xu, Jinwu Wei, Mengzhou Liao, Xiaobo Lu, Jiafeng Feng, Xiaoxi Li,
Yong Peng, Hongxiang Wei, Rong Yang, Dongxia Shi, Xixiang Zhang, Zheng Han*,
Zhidong Zhang, Guangyu Zhang*, Guoqiang Yu*, Xiufeng Han

*Corresponding author. Email: vitto.han@gmail.com (Z.H.); gyzhang@iphy.ac.cn (G.Z.); guoqiangyu@iphy.ac.cn (G.Y.)

Published 23 August 2019, *Sci. Adv.* **5**, eaaw8904 (2019)
DOI: 10.1126/sciadv.aaw8904

This PDF file includes:

Section S1. Crystal growth and characterization

Single crystals of Fe_3GeTe_2 were prepared by chemical vapor transport (CVT) method with iodine as the transport agent. High-purity (99.99%) Fe, Ge, and Te were milled into powder form with a stoichiometric molar proportion of 3:1:2 (Fe: Ge: Te) in an agate mortar. Mixture of starting materials and transport agent were then sealed in an evacuated quartz tube. The quartz tube was placed in a two-zone furnace, of which the gradient is between 800 ℃ and 625 ℃. The furnace temperature was first heated up to 625 ℃ with a rate of 1 ℃ per minute and then different sides were heated up to the set-point in 1 hour, respectively. The sample was maintained at the set-point for 4 days and was then cooled inside the furnace to room temperature. Single crystals of FGT formed at the colder side, as shown in Fig. S1.

As a comparison, the flux method was also used to grow the FGT single crystals. However, due to the low stoichiometric ratio of Fe elements (1.5% lower than that grown by CVT method, as shown in Fig. S2.), Curie temperature T_C of FGT single grown via flux-method is only 150 K, while T_C of those grown by CVT method is ~215 K, as summarized in Figs. S3-S7 and S9-S10.

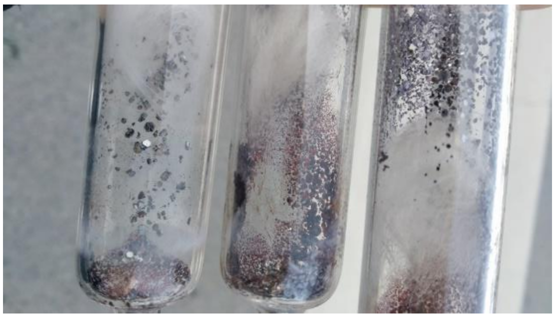

Fig. S1. Single crystals of FGT at the colder side in a sealed quartz tube (diameter of the tube is 1.5 cm). Photo Credit: Xiuxin Xia, Institute of Metal Research, Chinese Academy of Sciences.

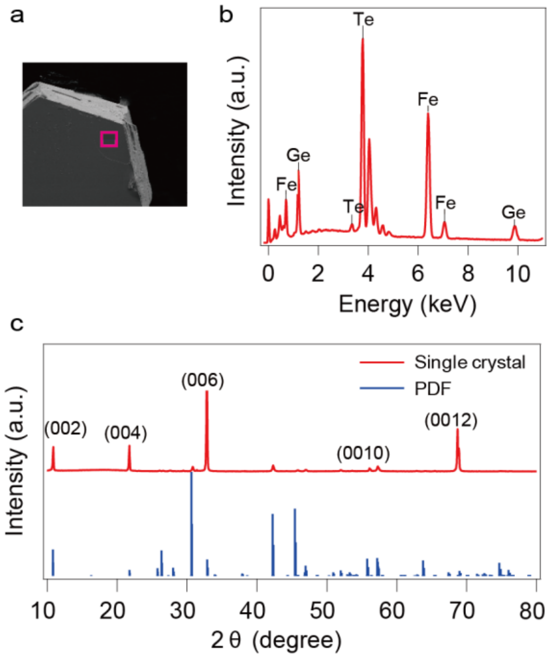

Fig. S2. Characterization of FGT single crystal grown by CVT method. a, Scanning electron microscope (SEM) image of the crystal, with its selected area characterized by energy dispersive spectroscopy (EDS), shown in b. The stoichiometric ratio detected by EDS suggests a Fe:Ge:Te of about 48.08 :16.68: 35.24 (atom %), Fe content is about 1.58 % higher than that grown by flux method. c, The X-ray diffraction (XRD) pattern of the as-grown single crystal.

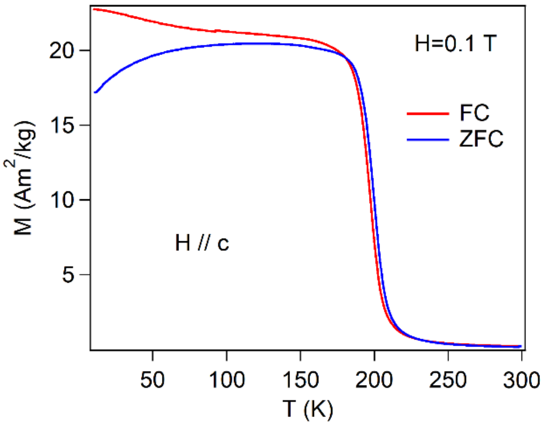

Fig. S3. Zero-field–cooling and field-cooling curves of the FGT crystals (grown by CVT) measured from 10 to 300 K with the external magnetic field (*H* = 0.1 T) parallel to the *c* axis.

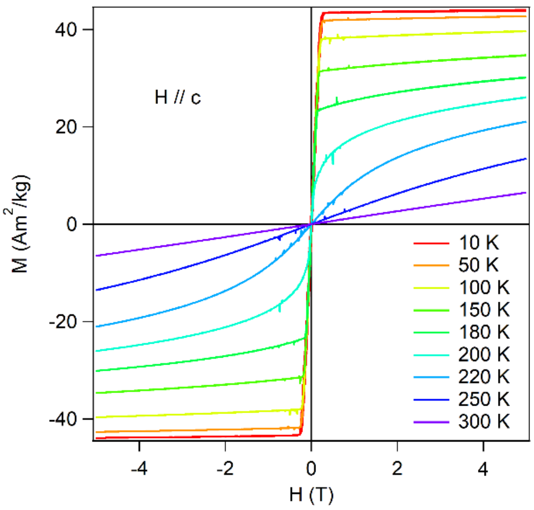

Fig. S4. Hysteresis loops measured of the FGT crystals (grown by CVT) at various temperatures with the external magnetic field parallel to the *c* axis.

Given the density of bulk FGT (7.3 g/cm^3), the bulk magnetization at 10 K is estimated to be 3.21×10^5 A/m.

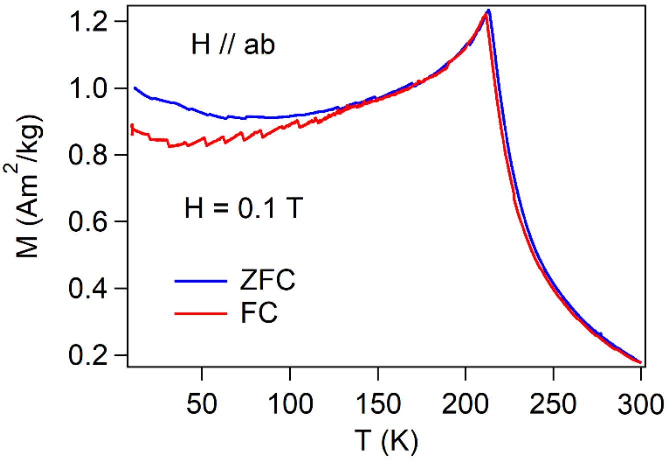

Fig. S5. Zero-field–cooling and field-cooling curves of the FGT crystals (grown by CVT method) measured from 10 to 300 K with the external magnetic field (*H* = 0.1 T) parallel to the *ab* plane.

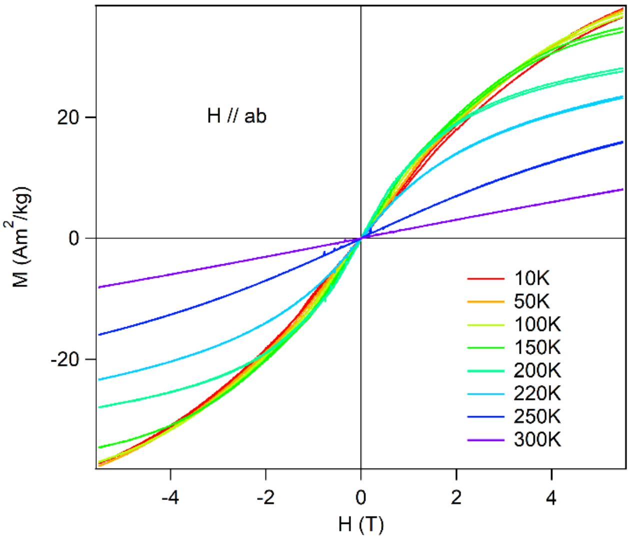

Fig. S6. Hysteresis loops of the FGT crystals (grown by CVT method) measured at various temperatures with the external magnetic field parallel to the *ab* plane.

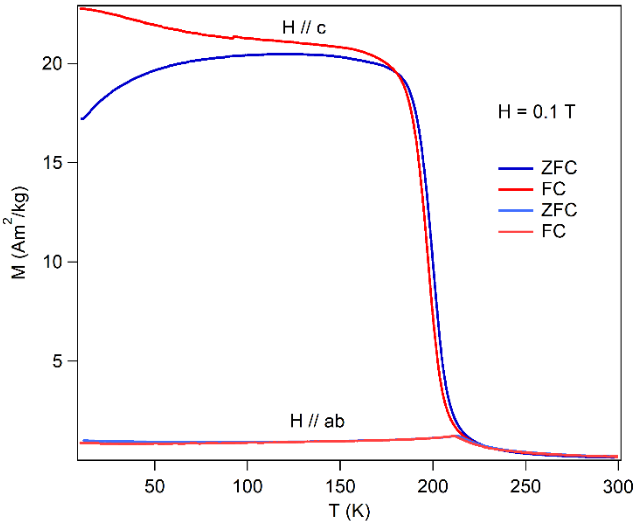

Fig. S7. Zero-field–cooling and field-cooling curves of the FGT crystals (grown by CVT) measured from 10 to 300 K with the external magnetic field (*H* = 0.1 T) parallel to the *c* axis and the *ab* plane.

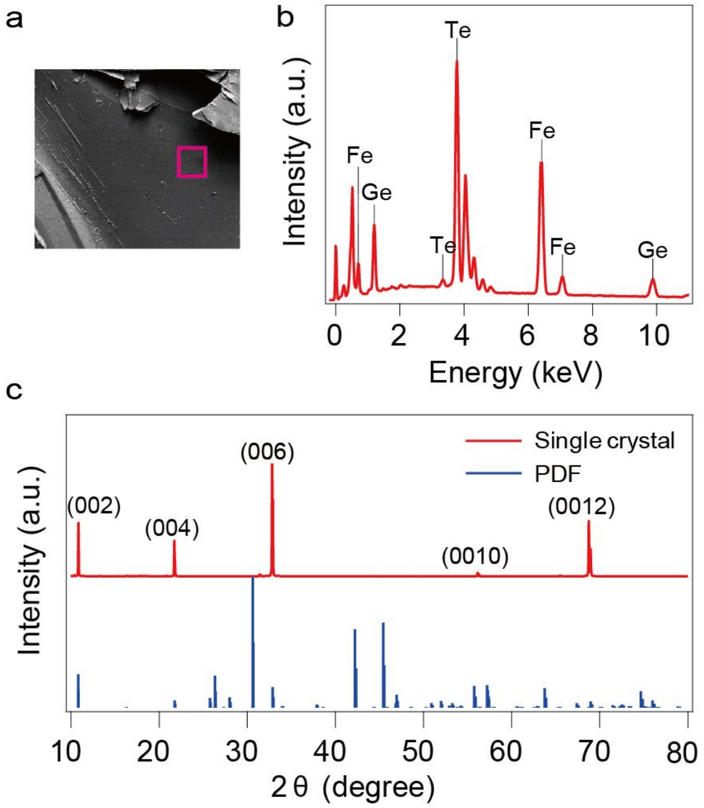

Fig. S8. Characterization of FGT single crystal grown by flux method. a, SEM image of the crystal, with its selected area characterized by EDS, shown in b, The stoichiometric ratio detected by EDS suggests a Fe:Ge:Te of about 46.50 :17.69: 35.82 (atom %). c, The XRD pattern of the as-grown single crystal.

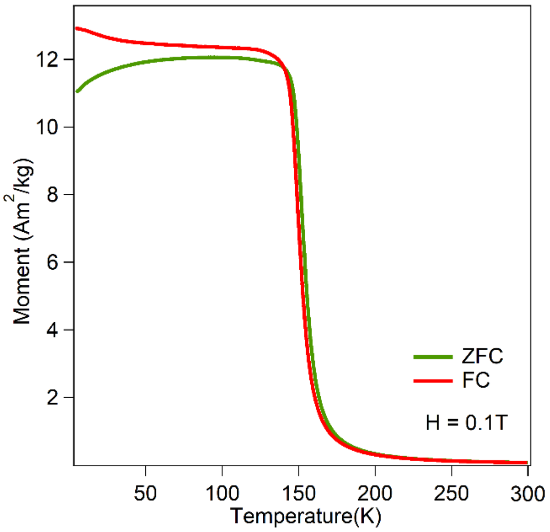

Fig. S9. Zero-field–cooling and field-cooling curves of the FGT crystals (grown by flux method) measured from 10 to 300 K with the external magnetic field (*H* = 0.1 T) parallel to the *c* axis.

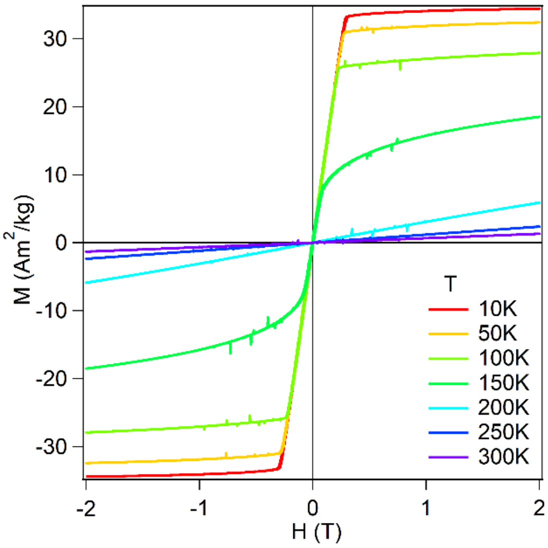

Fig. S10. Hysteresis loops measured of the FGT crystals (grown by flux method) at various temperatures with the external magnetic field parallel to the *c* axis.

Section S2. Exfoliation of FGT thin flakes and fabrication of FGT/Pt bilayer devices

We adopted the famed scotch tape method and obtained isolated thin FGT layers from the bulk materials by polydimethylsiloxane (PDMS) assisted exfoliation. The thickness of the FGT layers was identified by optical image and further confirmed by atomic force microscopy. The main challenge is transferring thin FGT layers on our desirable substrates. Here we developed two strategies (as shown in Fig. S11, process i and ii). The first is the scratching method. We re-exfoliated few-layer FGT on SiO_2 substrate through our home-made transfer station. The FGT layers were re-exfoliated during scratching process and we could obtain few-layer FGT flakes with freshly-cleaved ultra-clean surface and the surface roughness was 0.4 nm (as shown in Fig. S12a-b). However, the sizes of the obtained flakes were relatively small and this process could accidentally form wrinkles on the target flakes. The second one was PPC assisted process as thin FGT flakes on PDMS were covered onto PPC surface and further heated at 80 - 90 °C, so that the FGT flakes could be transferred onto PPC film totally. By this means, we could further transfer FGT layers onto other substrates casually. This process was damage-free but was left with more residues on the surface and the surface roughness was measured to be around 2.8 nm (Fig. S12c).

We immediately transferred the FGT/SiO_2 sample into a magnetic sputtering system and deposited a 6 nm-thick Pt layer (or 6 nm/1.5 nm Ta/Pt layer) with a background vacuum of below 8×10^{-7} Pa. The deposition rate was 0.94 Å/s at a power of 120 W and a pressure of 0.08 Pa. The obtained SiO_2/FGT/Pt(or Ta/Pt) bilayer is air-stable and this could confirm the subsequent fabrication process.

The Pt/FGT bilayer was patterned into a Hall-bar geometry by standard e-beam lithography (EBL) process and excrescent areas were etched by ion milling. Finally, electrodes were patterned by EBL and deposited with Ti(3 nm)/Au(50 nm) by e-beam evaporation (as shown in Fig. S11 and Fig. S13).

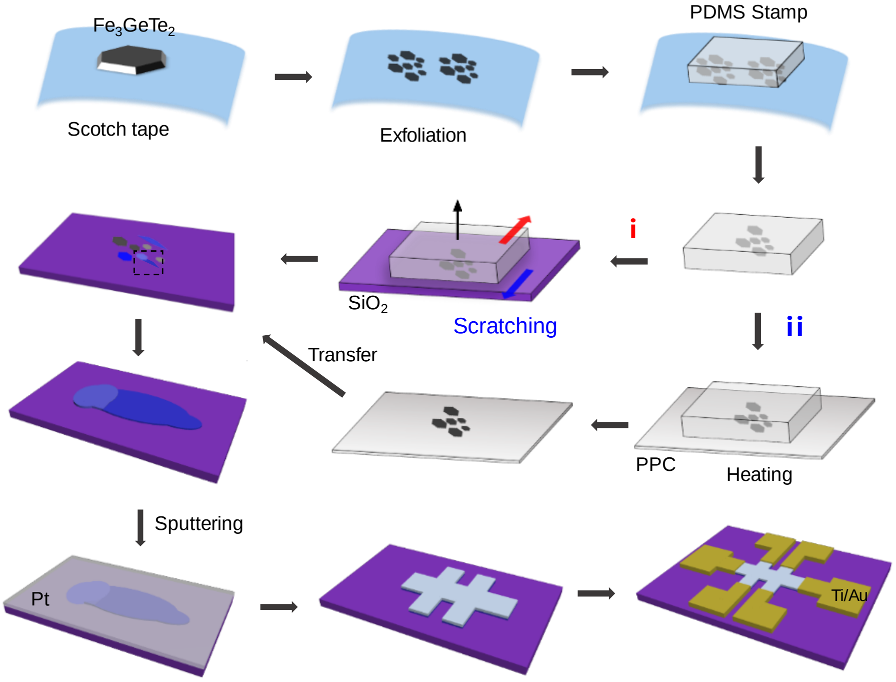

Fig. S11. Schematic view of FGT exfoliation, transfer, and device fabrication process.

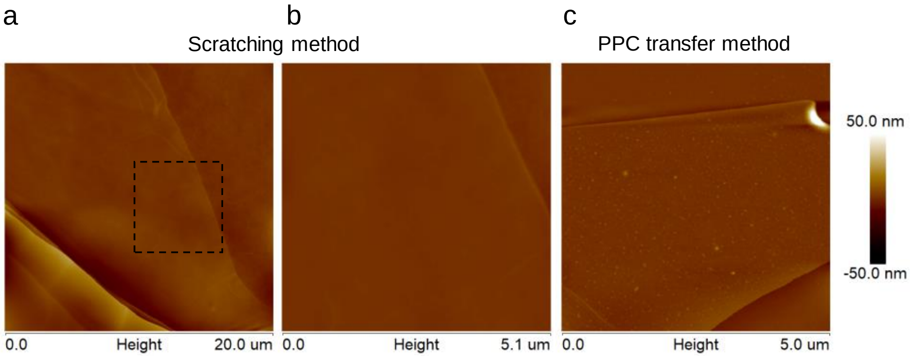

Fig. S12. Atomic force microscopy image of the obtained FGT flakes on SiO_2 substrate through two strategies. a-b. Scratching method. c. PPC transfer method.

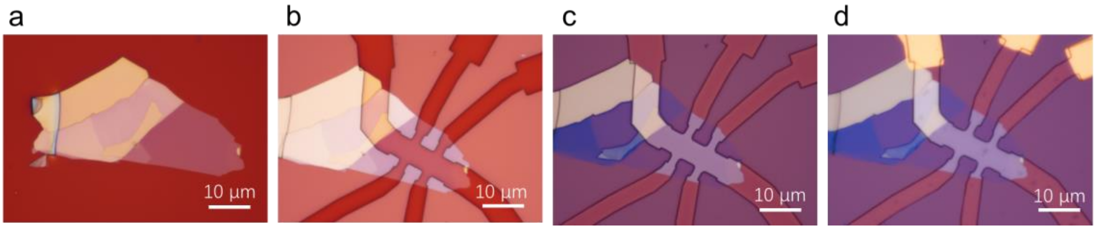

Fig. S13. Optical image of the device fabrication process. a. FGT/Pt bilayer. b. Patterned FGT/Pt bilayer with Hall geometry. c. Etching the excrescent areas. d. Fabrication Ti/Au electrode.

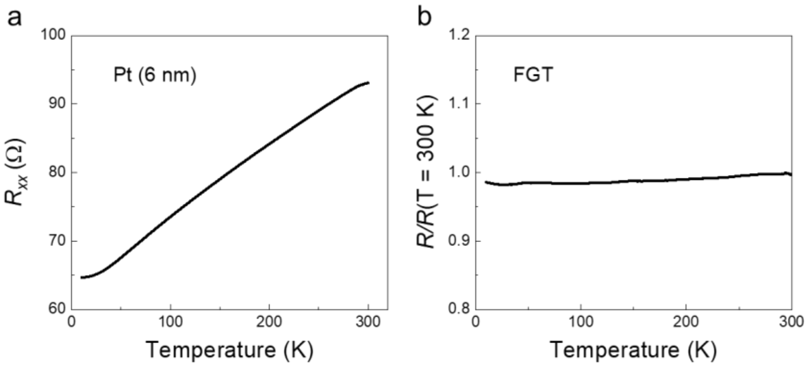

Fig. S14. Estimation of the temperature dependence of the resistance of FGT layers. a, Temperature dependence of longitudinal resistance (R_{xx}) for a 6 nm-thick Pt layer. The measured device is a patterned Hall bar on a Si/SiO_2 substrate, which is fabricated by using ultraviolet lithography. b, Temperature dependence of the resistance of FGT layers. The resistance is extracted by subtracting the transport contribution of the Pt layer. The resistance is normalized by the value at 300 K. The temperature dependence is similar to the FGT films with 4 to 6 layers[20].

Section S3. Correction of current-induced effective fields

In order to characterize the spin-orbit torque efficiency in the FGT/Pt system, we performed the harmonic measurements, as described in the main text. In this manner, the effective fileds corresponding to the damping-like and field-like torques can be extracted. However, the parasitic thermal signal also exists since the a.c. current generates an oscillating thermal gradient, which generates a 2nd harmonic Hall voltage through anomalous Nernst effect and spin Seebeck effect(*33*, *34*). As shown in Fig. S15, since the Hall voltage is measured in the transverse (y) direction, the thermal effects (anomalous Nernst and spin Seebeck signal have the same symmetry) contribute the voltage signals when the field scanned in longitudinal (x) direction.

In this work, the contribution from the thermal effect is carefully removed. First, a second harmonic measurement was performed with a large field which could saturate the magnetization. The difference between the second-order voltages at $+M_x$ and $-M_x$ were extracted to quantify the thermal voltage ($\Delta V^{2\omega}_{\mathrm{thermal}}$) which was proportional to the M_x. Meanwhile, first-order anomalous Hall voltage could be used to calibrate the angle between the magnetization and z direction because the anomalous Hall voltage is proportional to the M_z. Therefore, the measured 1st and 2nd order harmonic voltages can be expressed by

$$V^{1\omega}_{\mathrm{meas}}(H_L) = \Delta V^{1\omega}_{\mathrm{AHE}} \cos\theta\,(H_L) + V^{1\omega}_{\mathrm{offset}}$$

$$V^{2\omega}_{\mathrm{meas}}(H_L) = V^{2\omega}_{\mathrm{torque}}(H_L) + \Delta V^{2\omega}_{\mathrm{thermal}} \sin\theta\,(H_L) + V^{2\omega}_{\mathrm{offset}}$$

where θ is the angle between magnetization and $+z$ direction, $\Delta V^{1\omega}_{\mathrm{AHE}}$ is the anomalous Hall voltage, $V^{2\omega}_{\mathrm{torque}}(H_L)$ is the 2nd order harmonic voltage contributed by spin-orbit torque effective field. The data after the subtraction of the $\Delta V^{2\omega}_{\mathrm{thermal}} \sin\theta\,(H_L)$ component are shown in the Fig. 3b in main text. The thermal contribution is not very pronounced since the conductivity of the FGT and Pt are close to each other.

In the harmonic measurements, several parameters of the material also change because of Joule heating. In our system, the saturation magnetization (M_s), the magnetic anisotropy ($K_u = 1/2M_sH_k$) and the anomalous Hall resistance (R_{AHE}) can influence the effective field estimation. According to the temperature dependence of resistance, we estimated that the device temperature could increase up to 47 K (ΔT = 37 K) when applying a 3 mA current. According to the reference(*34*), the form of M_S, $K_{u,}$ and R_{AHE} could be given by:

$$M_s(T) = M_s(1 - \alpha\Delta T)$$

$$K_u(T) = K_u(1 - \beta\Delta T)$$

$$R_{AHE}(T) = R_{AHE}(1 - \gamma\Delta T)$$

The effective field induced by current could be revised by

$$\Delta H_{T(L)} \approx \Delta H^{c}_{T(L)}\left[1 - \frac{1}{4}\left(\gamma + \frac{D'}{D}\right)\Delta T\right]$$

where $D' = \frac{2K_u}{M_s}(\alpha - \beta) + 4\pi M_s\alpha$ and $D = \frac{2K_u}{M_s} - 4\pi M_s\alpha$. $\Delta H_{T(L)}$is the effective field induced by current without considering the changing parameters while $\Delta H^{c}_{T(L)}$ is corrected by considering the change of magnetic properties due to thermal effect. Based on the temperature dependence of these parameters, we could roughly estimate that

$$\alpha\Delta T = 0.047$$

$$\beta\Delta T = 0.150$$

$$\gamma\Delta T = 0.012$$

After the calibration, we could obtain that the $\Delta H_{\mathrm{T(L)}}$ is larger than $\Delta H^{\mathrm{c}}_{\mathrm{T(L)}}$ by less than 3% for the temperature increase of 37 K.

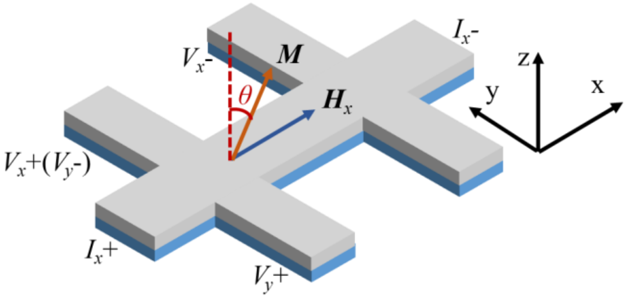

Fig. S15. Schematic diagram of measurement setup and coordinate system.

Besides, we have considered the contribution from the Oersted field. The Oersted field indeed contributes to the measurement of transverse effective field. According to the Ampere's law, the y-oriented Oersted field is given by $\mu_0 H_{\mathrm{Oe}}/J_{\mathrm{e}} = \mu_0 t/2$, where t = 6 nm is the thickness of the heavy metal. The estimated Oersted field is $\mu_0 H_{\mathrm{Oe}}/J_{\mathrm{e}} =$ 0.4 mT/(10^7 A/cm^2), which is much smaller than the transverse effective field in both Pt and Ta devices.

Section S4. Current-driven switching at different temperatures

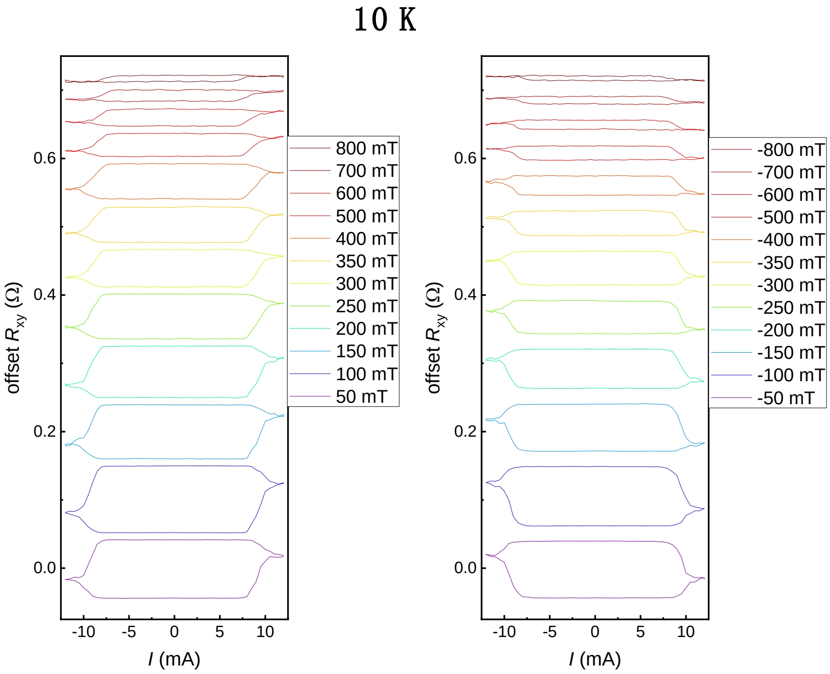

Fig. S16. Current-driven switching at 10 K.

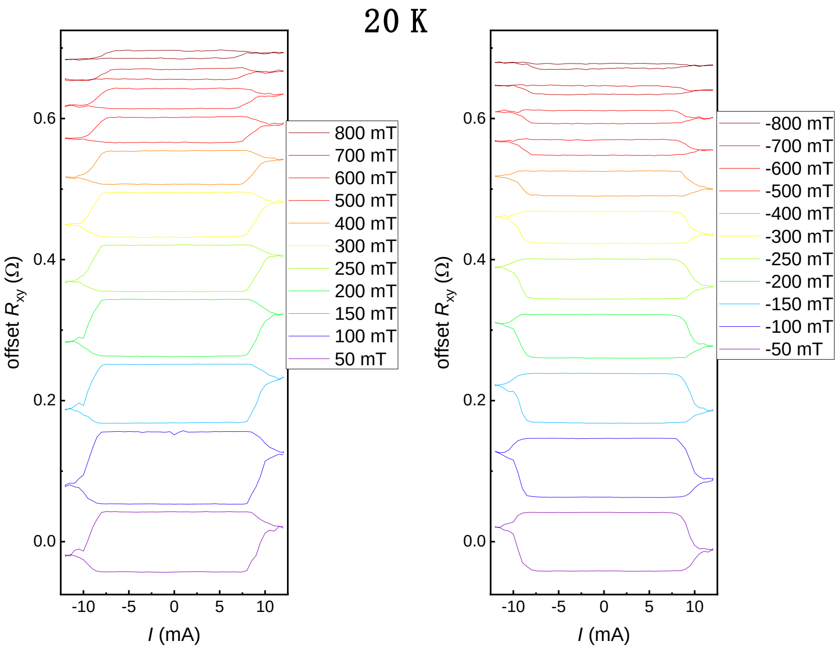

Fig. S17. Current-driven switching at 20 K.

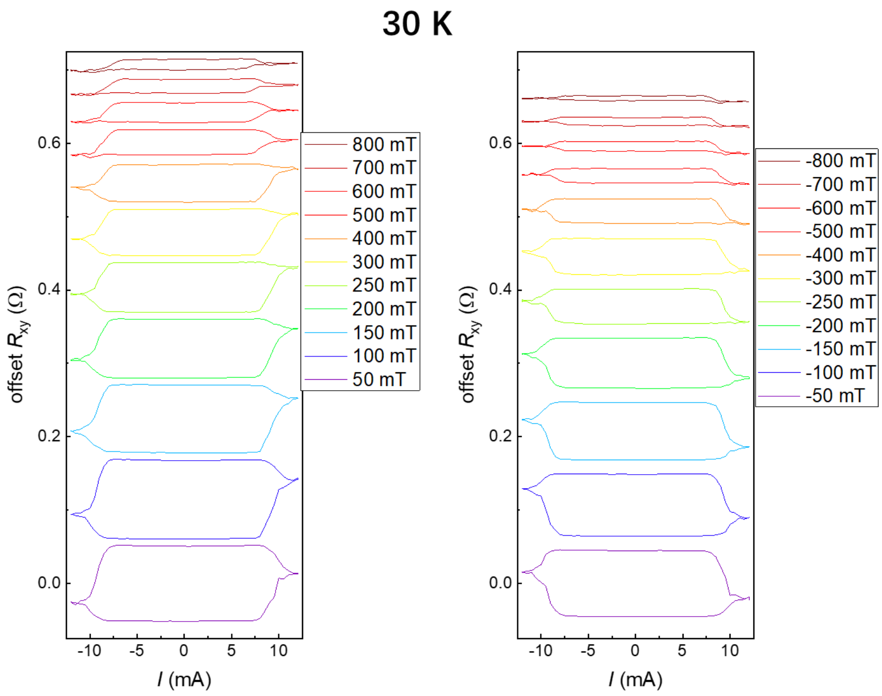

Fig. S18. Current-driven switching at 30 K.

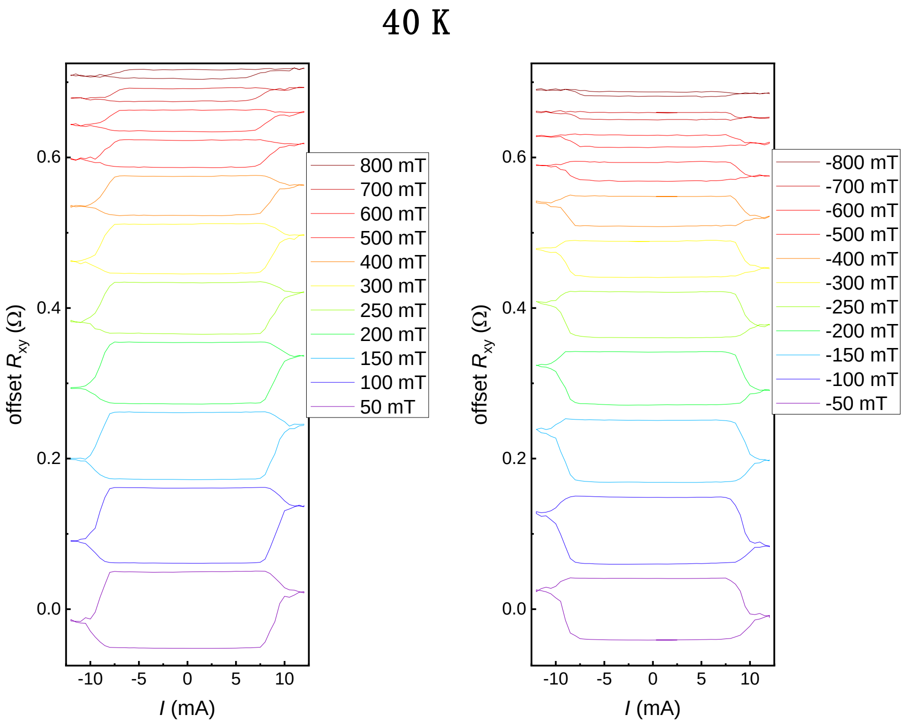

Fig. S19. Current-driven switching at 40 K.

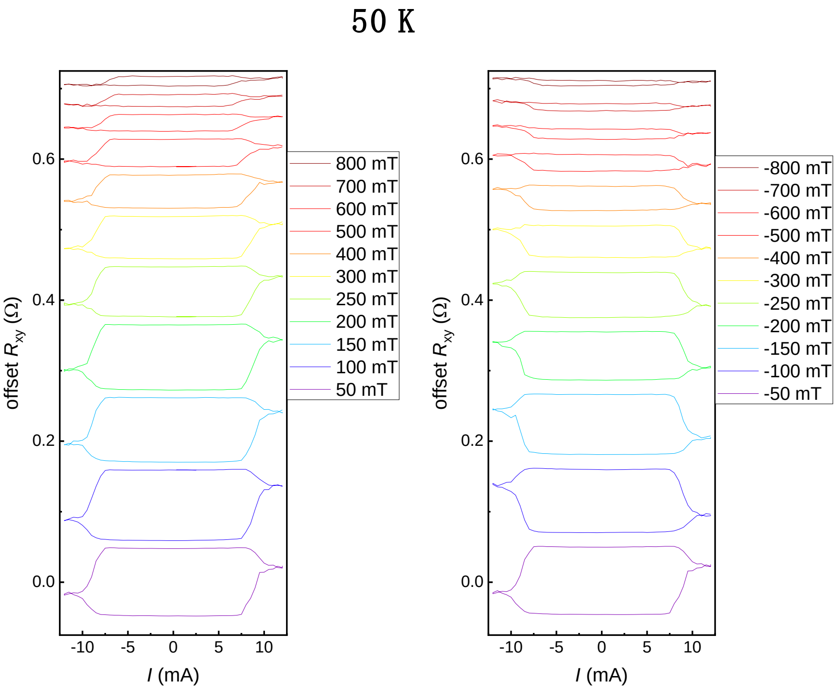
50 K

Fig. S20. Current-driven switching at 50 K.

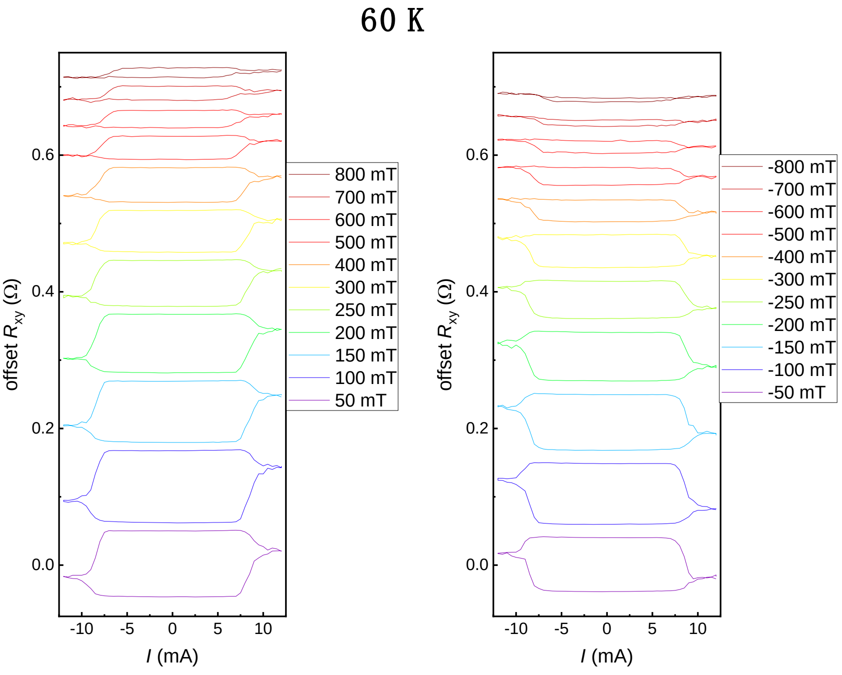
60 K

Fig. S21. Current-driven switching at 60 K.

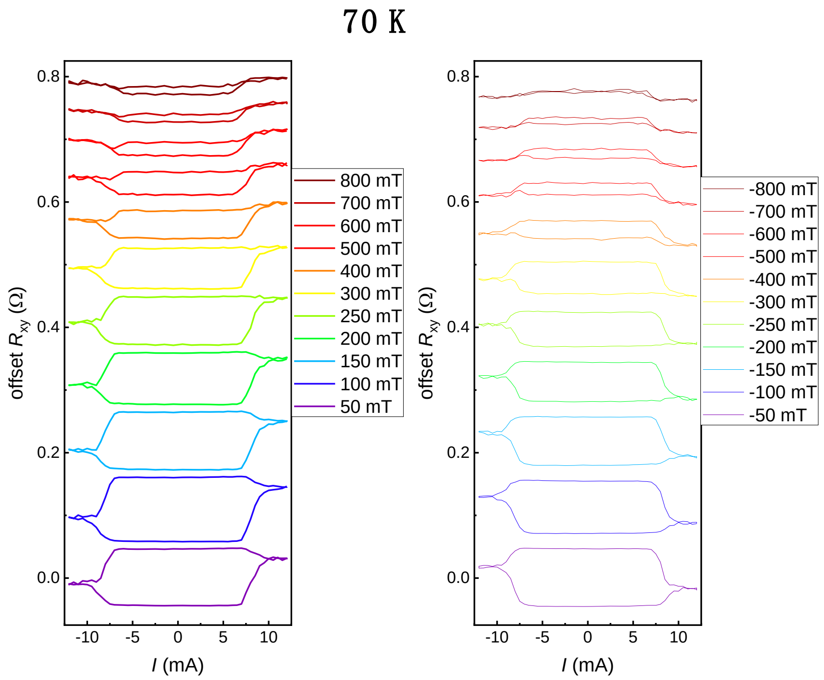

Fig. S22. Current-driven switching at 70 K.

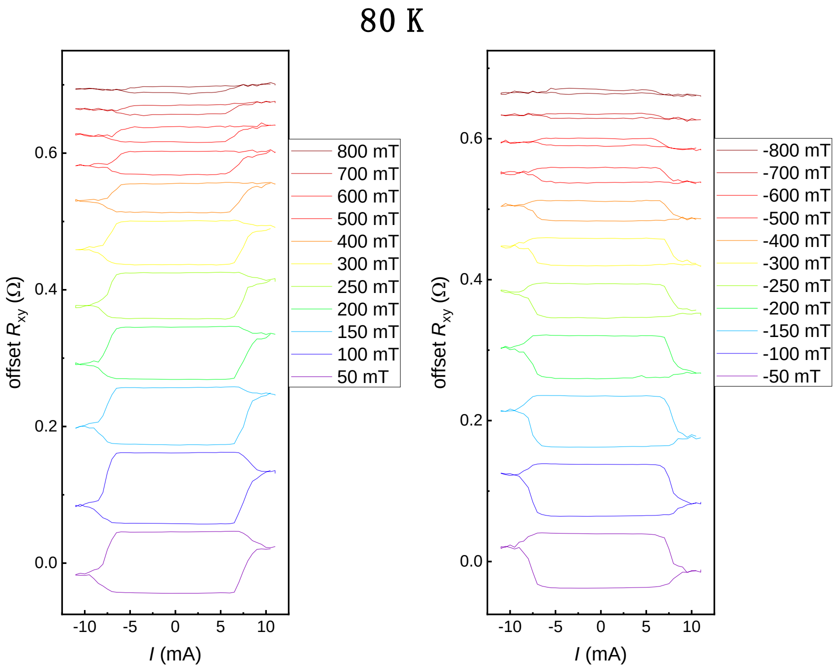

Fig. S23. Current-driven switching at 80 K.

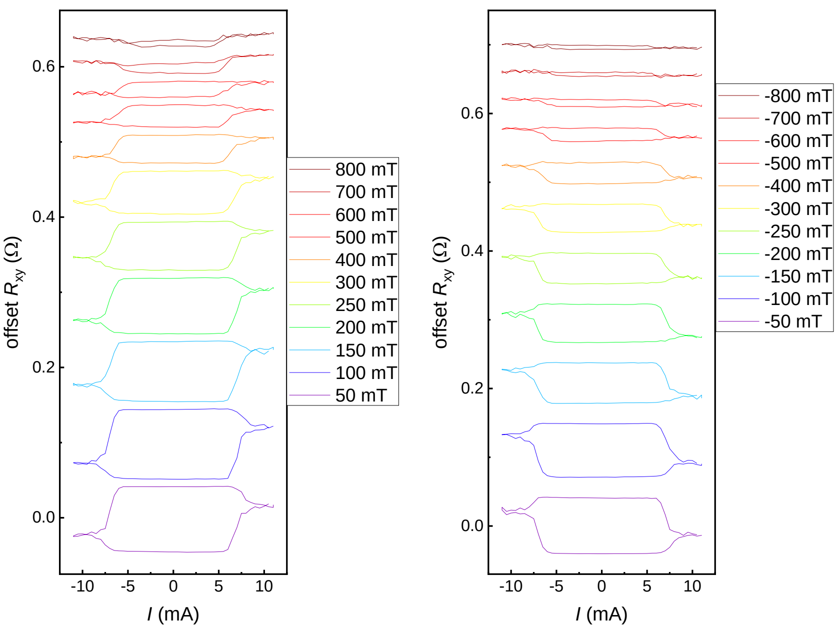
90 K

Fig. S24. Current-driven switching at 90 K.

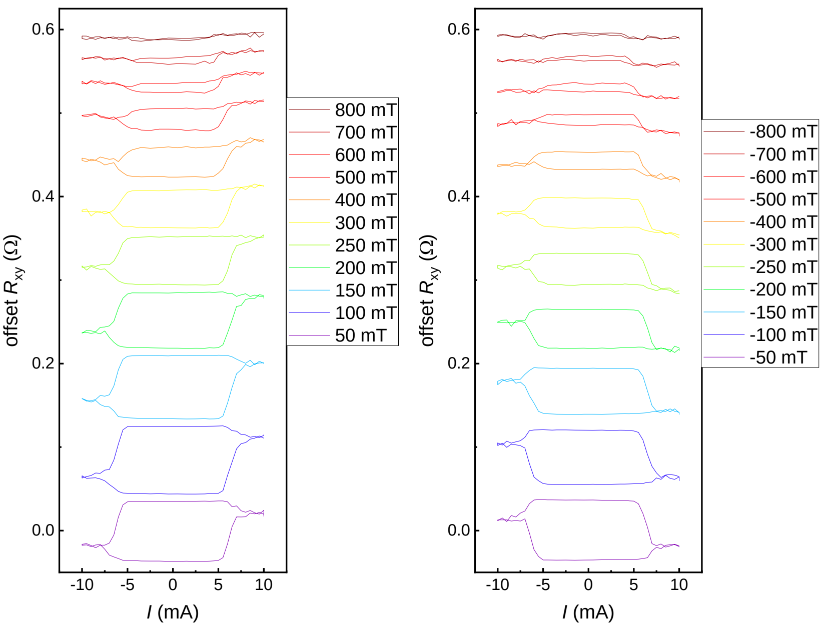
100 K

Fig. S25. Current-driven switching at 100 K.

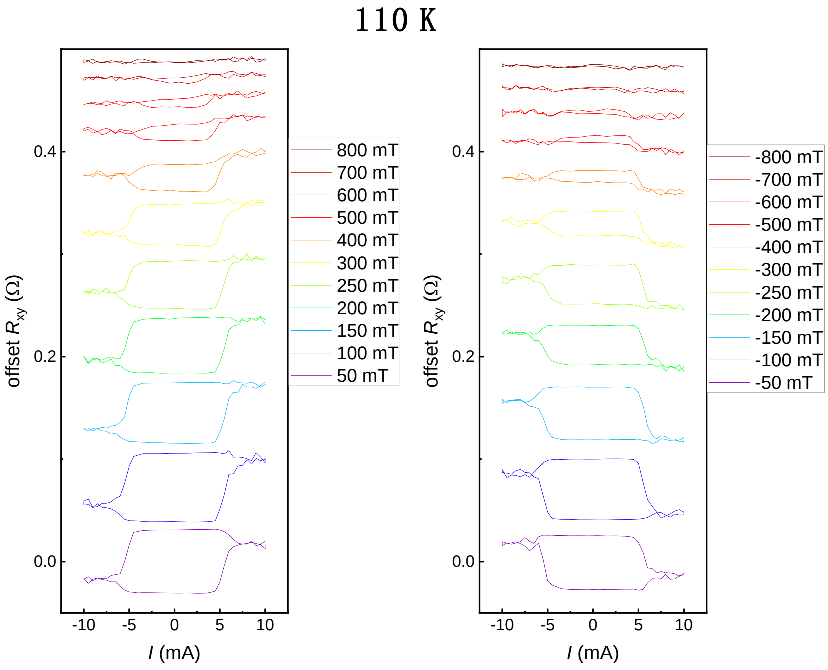

Fig. S26. Current-driven switching at 110 K.

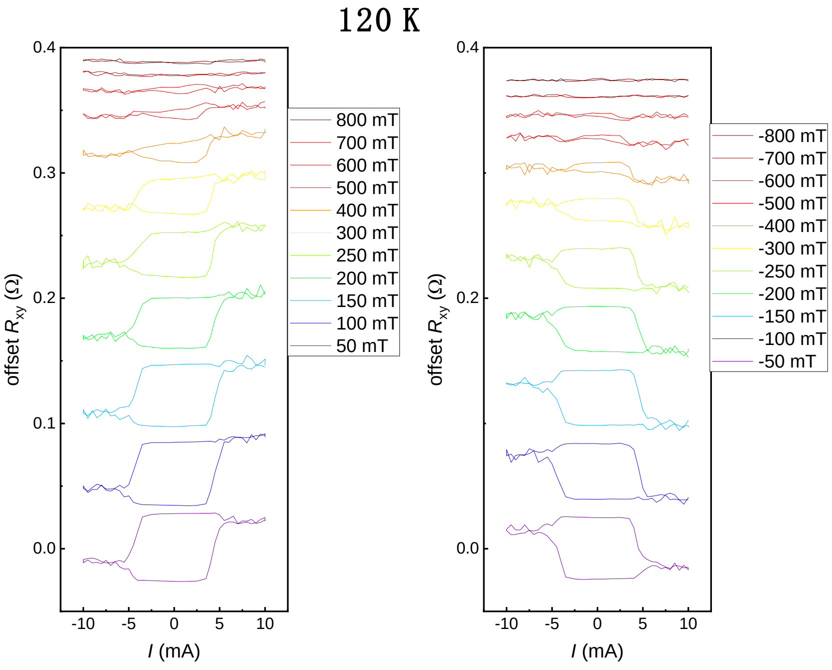

Fig. S27. Current-driven switching at 120 K.

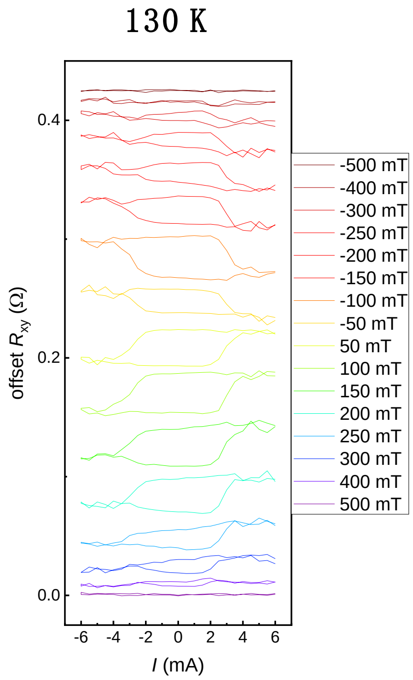

Fig. S28. Current-driven switching at 130 K.

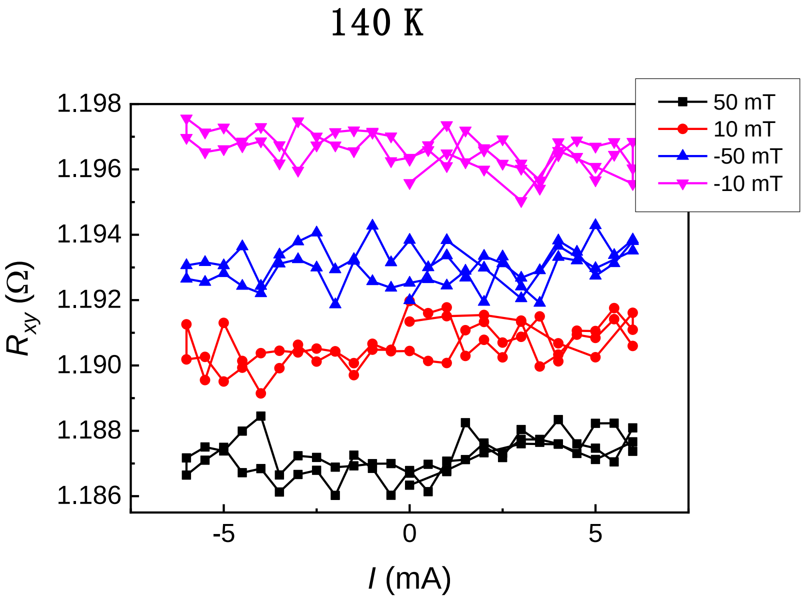

Fig. S29. R_{xy} as a function of current under different in-plane magnetic field at 140 K.

Section S5. Current-driven magnetization switching

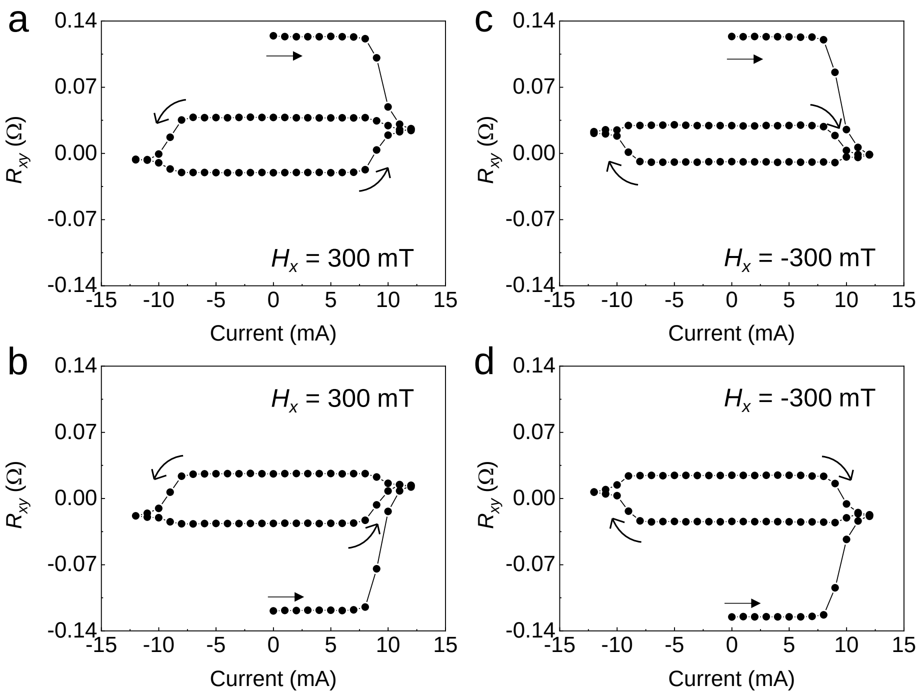

Fig. S30. Current-driven magnetization switching for different initial states. a,c, Current-driven magnetization switching for the initial state of $M_z > 0$. The applied in-plane magnetic fields are positive and negative, respectively. During the switching, the anomalous Hall resistance does not reach the maximum Hall resistance, indicating the incomplete switching. This is ascribed to the current-induced thermal effect, which prevents using a large current to accomplish the complete switching before the temperature approaches the Curie temperature. b,d, Current-driven magnetization switching for the initial state of $M_z < 0$. The applied in-plane magnetic fields are positive and negative, respectively.

Section S6. Current-driven magnetization switching and measurement of effective fields corresponding the current-induced torques

We also carried out experiments to characterize the current-induced switching (Fig. S31) and effective fields (Fig. S32) in the FGT/Ta sample. Figure S31 shows the current-driven magnetization switching. Compared with the switching in the FGT/Pt device, we obtain similar switching behavior but with opposite switching polarity due to the opposite sign of the spin Hall angle in Ta. Figure S32 shows the first and second harmonic voltages under longitudinal (H_L) and transverse (H_T) external magnetic fields, which are fitted by parabolic and linear functions, respectively. The obtained effective fields per unit current density are $\Delta H_{\mathrm{L}} = 9.1 \pm 2.1$ mT/(10^7 A/cm^2) and $\Delta H_{\mathrm{T}} = 24.0 \pm 3.0$ mT/(10^7 A/cm^2), respectively. If we assume that the M_s of FGT/Pt and FGT/Ta sample are the same, we can compare the spin torque efficiency values of FGT/Pt and FGT/Ta samples through comparing their effective fields. The absolute value of damping-like spin torque efficiency in the FGT/Pt sample is larger than that in the FGT/Ta sample. The field-like one in the FGT/Pt sample is comparable to that in the FGT/Ta sample. However, in the previous works, the absolute values of damping-like and field-like spin torque efficiency in the Pt-based sample are typically smaller than those in the Ta-based samples (*27*, *35*). We speculate that the interfacial spin transparency (T_{int}) of the FGT/Ta sample may be smaller than that of the FGT/Pt sample. We can also estimate the upper limit value of M_s based on the damping-like effective field obtained in the FGT/Ta sample. If we assume that the spin torque efficiency in Ta is less than 0.16, the upper limit value of M_s is approximately 1.2×10^5 A/m, which is also smaller than the bulk value (3.21×10^5 A/m).

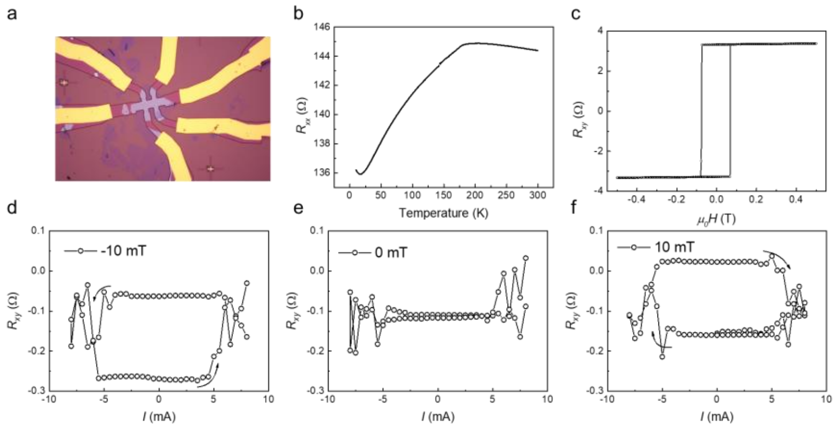

Fig. S31. Current-driven switching in an FGT/Ta bilayer. a, A fabricated device with FGT/Ta bilayer structure. b, Temperature dependence of the device resistance. c, Hall resistance as a function of out-of-plane magnetic field at 10 K. The square hysteresis loop indicates a good perpendicular magnetic anisotropy. d-f, Current-driven magnetization switching with an in-plane magnetic field of −10 mT, 0 mT, and 10 mT at 10 K. The switching polarity is opposite to those for FGT/Pt bilayer, which is consistent with the fact that the spin Hall angle of the Ta is opposite to the Pt. It should be noted that, for the switching from $M_z > 0$ to $M_z < 0$, the anomalous Hall resistance does not reach the maximum value (see main text). This can be similarly explained by thermal effect like the case for the FGT/Pt device. The switching percentage is smaller than that of the Pt layer, which is likely because the Ta has a larger resistivity (typically one order larger than Pt) and the current mainly passes through the FGT layer, resulting in a smaller SOT in the FGT/Ta device.

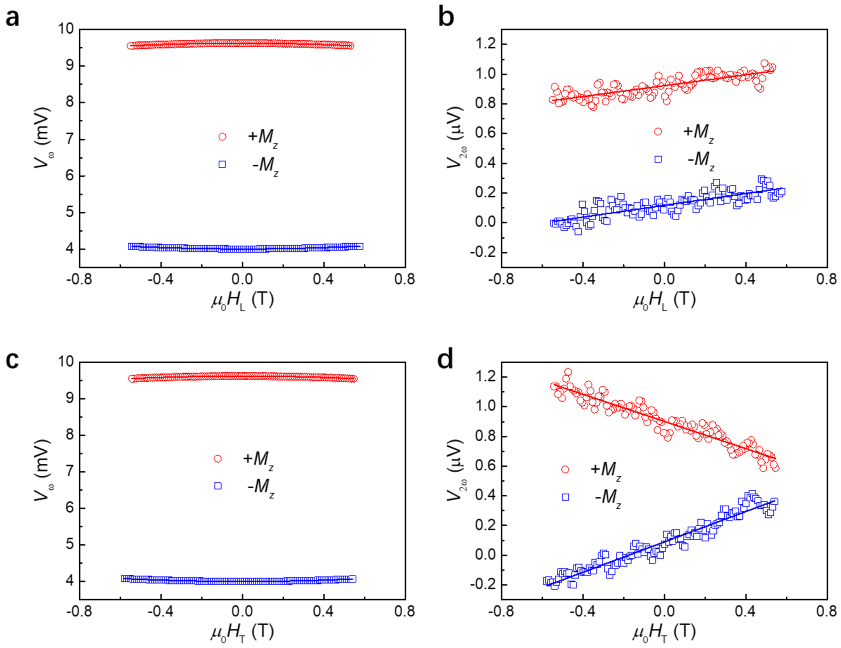

Fig. S32. Characterization of the current-induced effective fields in an FGT/Ta device. a,b, First and second harmonic voltages for the longitudinal effective field. H_L is the applied longitudinal magnetic field along the current direction (*x* axis). c,d, First and second harmonic voltages for the transverse effective field. H_T is the applied transverse magnetic field transverse to the current direction (*y* axis).

Section S7. Temperature dependence of PMA

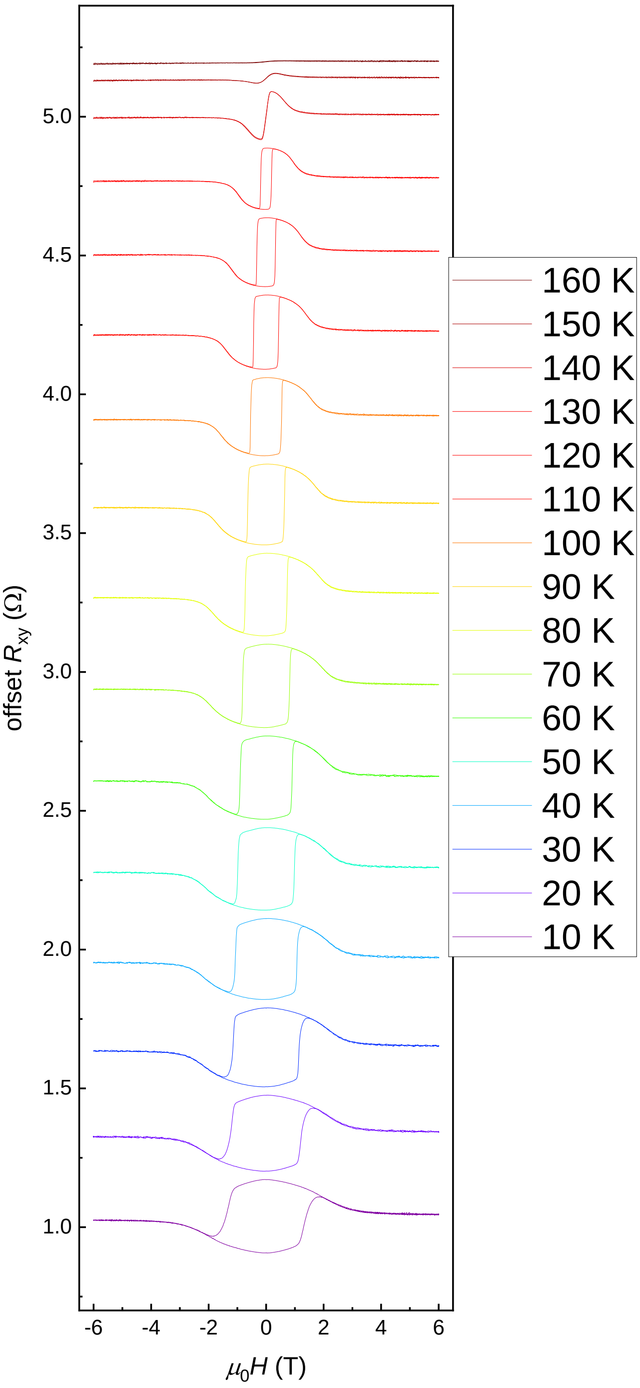

Fig. S33. Hall resistance as a function of in-plane magnetic field. The effective anisotropy field can be determined as shown in Fig. S34.

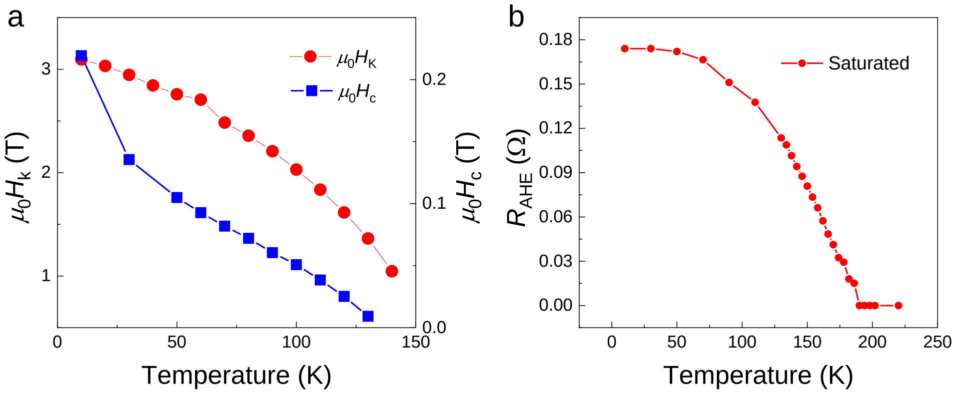

Fig. S34. Temperature dependence of effective anisotropy field ($\mu_0 H_k$), coercivity ($\mu_0 H_c$), and saturation anomalous Hall resistance.